drones

MDPI

Article

Using Multi-Sensor Data Fusion Techniques and Machine Learning Algorithms for Improving UAV-Based Yield Prediction of Oilseed Rape

Hongyan Zhu [1,2,*], Shikai Liang [1,2], Chengzhi Lin [1,2], Yong He [3,*] and Jun-Li Xu [4]

[1] Guangxi Key Laboratory of Brain-Inspired Computing and Intelligent Chips, School of Electronic and Information Engineering, Guangxi Normal University, Guilin 541004, China; skliang-gxnu@foxmail.com (S.L.); chengzhilin@stu.gxnu.edu.cn (C.L.)
[2] Key Laboratory of Integrated Circuits and Microsystems, Education Department of Guangxi Zhuang Autonomous Region, Guangxi Normal University, Guilin 541004, China
[3] College of Biosystems Engineering and Food Science, Zhejiang University, Hangzhou 310058, China
[4] School of Biosystems and Food Engineering, University College Dublin (UCD), Belfield, 4 Dublin, Ireland; junli.xu@ucd.ie
* Correspondence: hyzhu-zju@foxmail.com (H.Z.); yhe@zju.edu.cn (Y.H.)

Abstract: Accurate and timely prediction of oilseed rape yield is crucial in precision agriculture and field remote sensing. We explored the feasibility and potential for predicting oilseed rape yield through the utilization of a UAV-based platform equipped with RGB and multispectral cameras. Genetic algorithm–partial least square was employed and evaluated for effective wavelength (EW) or vegetation index (VI) selection. Additionally, different machine learning algorithms, i.e., multiple linear regression (MLR), partial least squares regression (PLSR), least squares support vector machine (LS-SVM), back propagation neural network (BPNN), extreme learning machine (ELM), and radial basis function neural network (RBFNN), were developed and compared. With multi-source data fusion by combining vegetation indices (color and narrow-band VIs), robust prediction models of yield in oilseed rape were built. The performance of prediction models using the combination of VIs (RBFNN: R_{pre} = 0.8143, RMSEP = 171.9 kg/hm^2) from multiple sensors manifested better results than those using only narrow-band VIs (BPNN: R_{pre} = 0.7655, RMSEP = 188.3 kg/hm^2) from a multispectral camera. The best models for yield prediction were found by applying BPNN (R_{pre} = 0.8114, RMSEP = 172.6 kg/hm^2) built from optimal EWs and ELM (R_{pre} = 0.8118, RMSEP = 170.9 kg/hm^2) using optimal VIs. Taken together, the findings conclusively illustrate the potential of UAV-based RGB and multispectral images for the timely and non-invasive prediction of oilseed rape yield. This study also highlights that a lightweight UAV equipped with dual-image-frame snapshot cameras holds promise as a valuable tool for high-throughput plant phenotyping and advanced breeding programs within the realm of precision agriculture.

Keywords: data fusion; machine learning algorithms; oilseed rape; remote sensing; unmanned aerial vehicle (UAV); yield prediction

check for updates

Citation: Zhu, H.; Liang, S.; Lin, C.; He, Y.; Xu, J.-L. Using Multi-Sensor Data Fusion Techniques and Machine Learning Algorithms for Improving UAV-Based Yield Prediction of Oilseed Rape. *Drones* **2024**, *8*, 642. https://doi.org/10.3390/drones8110642

Academic Editor: Pablo Rodríguez-Gonzálvez

Received: 31 July 2024
Revised: 30 October 2024
Accepted: 31 October 2024
Published: 5 November 2024

1. Introduction

Crop yield hinges on the growth and differentiation of crops, as well as the distribution and accumulation of photosynthetic products, constituting a pivotal area of study in crop science. The precise and early prediction of crop yield consistently stands as one of the most important areas of investigation in precision agriculture [1]. Oilseed rape (*Brassica napus* L.) is a significant global oil crop that can be used to produce high-quality feed, cooking oil, dishes, biodiesel, and so on [2,3]. The timely and accurate yield prediction of oilseed rape is of guiding significance for agricultural producers to carry out cultivation, breeding, production, and sales activities reasonably and effectively. Conventionally, the prevalent approaches for estimating crop yield involved establishing correlations between agronomic or climatic factors and crop yields through manual surveys or employing statistical analysis methods [4,5], which were not uniform, time-consuming and laborious. At present, the large-scale commercial breeding of oilseed rape has led to a sharp increase in the combination of breeding materials. It was difficult to ensure the uniformity and timeliness of data for estimating yield. Therefore, there is an urgent need to devise a swift, dependable, and non-invasive method capable of accurately forecasting oilseed rape yields on a field scale.

Remote sensing is a real-time means of obtaining phenotypic information for crops, with a large monitoring range and low damage to crops, so it was widely used in agricultural information acquisition [4]. The demand for the timely and non-destructive evaluation of crop yield across diverse scales has resulted in the growing acceptance of remote sensing technologies [5]. Utilizing unmanned aerial vehicles (UAVs) for remote sensing has overcome the limitations associated with satellites, aircraft, and ground-based platforms. UAVs enable frequent flight tests at specific locations and times, facilitating the monitoring of crops through multi-scale and multi-temporal images. This capability allows for the observation of fine-scale spatial patterns in a more efficient manner [6]. UAVs equipped with sensors offer advantages such as high resolution, flexibility, and cost-effectiveness, making them well suited for integration with remote sensing technology. The utilization of low-altitude remote sensing by UAVs, equipped with spectral imaging sensors, in field-based crop phenotyping has gained prominence and is on the rise [7]. A number of studies have been conducted on crop yield prediction models based on RGB cameras or multispectral cameras by UAV-based platforms. Models were constructed by plant height, leaf area index, growth period length, chlorophyll content, biomass, and other physiological and biochemical indicators, as well as spectral reflectance and vegetation indices obtained by remote sensing platforms [3,8]. Li et al. [6] used the leaf abundance and vegetation indices of oilseed rape to predict yield with unmanned aircraft system visual-band imagery. More research has focused on the spectral reflectance characteristics specific to crops, utilizing the construction of remote sensing quantitative models that incorporate multiple vegetation indices to achieve crop yield prediction [9,10]. For example, Lukas et al. [11] utilized an UAV platform equipped with a multispectral camera to obtain a good prediction model for oilseed rape yield according to the color vegetation indices including blue normalized difference vegetation index (BNDVI) and normalized difference yellowness index (NDYI). Zhang et al. [12] achieved predictions of flowering number and yield based on spectral information and multispectral vegetation index obtained from multispectral cameras.

All of these have demonstrated the potential and feasibility of UAV-based platforms with imaging sensors for yield prediction. Additionally, the premise of large-scale application of the UAV remote sensing platform is to continuously improve the adaptability and accuracy of the yield prediction models. However, the prediction models of many studies were based on univariate modeling with a single vegetation index [12–14] or simple linear multivariate modeling such as multivariate linear regression (MLR) and partial least squares regression (PLSR) [15–17]. Multivariate-based vegetation index modeling was better than using a single vegetation index for predicting crop phenotypic information [18], and individual vegetation indices such as the normalized difference vegetation index (NDVI) may be saturated under moderate to high-biomass conditions or late crop growth stages [19,20]. As a high-density crop, it is essential to explore the sensitivity of other vegetation indices to yield an estimation of oilseed rape. Moreover, the above studies lack information mining of UAV remote sensing data and the application of advanced machine learning algorithms. It is especially crucial to dig out more vegetation indices and use a variety of advanced machine learning algorithms to increase the accuracy and robustness of predictive models [16].

Predicting the yield of oilseed rape presents challenges due to its distinct developmental stages such as seedling, bolting, flowering, and pod formation. The spectral characteristics vary in different periods, which increases the uncertainty of yield prediction [21]. In particular, the yellow flowers of the canopy during flowering reduced the accuracy of oilseed rape phenotypic prediction [21]. Choosing the appropriate period of oilseed rape is paramount for yield prediction. About 2/3 of the dry matter of oilseed rape is provided by green horns. The pod filling stage is the key growth stage for material synthesis and nutrient accumulation and is a substantial stage of oilseed rape reproductive growth. The final yield is determined by three crucial factors: the number of seeds per pod, the number of pods per plant, and the 1000-seed weight, as identified by Li et al. [22], who showed that the spectra at the pod filling stage by an ASD field portable spectrometer accurately predicted the yield of oilseed rape. Consequently, this research focused on the pod filling stage to predict the yield of oilseed rape, which can save manpower and material resources and reduce the number of flights of UAVs.

Currently, researchers have begun exploring the use of drones equipped with RGB cameras and multispectral sensors for crop yield estimation, significantly expanding the depth and breadth of agricultural remote sensing research. Unlike traditional methods that typically relied on a single sensor, this multi-sensor integration strategy captures abundant growth information, providing comprehensive data support for crop assessment [23,24]. By analyzing RGB images, researchers can identify crop growth stages, health status, and potential pest and disease issues. Meanwhile, multispectral cameras capture the spectral reflectance of the crops, helping to assess physiological conditions such as chlorophyll content and water status. This spectral data not only revealed crop growth dynamics but also reflected the impact of soil and environmental factors on crop growth, enabling high-precision growth assessment. By combining RGB and multispectral data, researchers can build more complex and accurate analytical models, which comprehensively evaluate crop growth potential, leading to more accurate yield predictions [25–27]. This is of great significance for optimizing the crop yield estimation process and providing scientific support for decision-making in modern agricultural management.

Therefore, this study aims to investigate the feasibility of estimating oilseed rape yield using a dual-camera platform (RGB and multispectral cameras) mounted on drones. Through the fusion of RGB and multispectral camera data, we will systematically analyze the complementarity of these two sensor types in capturing oilseed rape growth information. This analysis will focus particularly on the pod filling stage to explore the relationship between growth characteristics and yield, thereby improving the accuracy of yield predictions. The specific objectives are as follows: (1) based on the full-band information provided by the multispectral camera, we will establish an effective oilseed rape yield prediction model using various machine learning algorithms (such as the extreme learning machine, support vector machine, and partial least squares regression); (2) through systematic analysis and comparison, we will identify the best vegetation indices (VIs) for yield estimation and multivariate fusion modeling to enhance model performance; (3) we will compare the effectiveness of models based on single-sensor (multispectral camera) versus dual-sensor fusion (RGB and multispectral cameras) in yield prediction, analyzing the degree to which data fusion improves prediction accuracy; (4) by selecting appropriate variable selection algorithms, we will identify effective wavelengths (EWs) and optimal VI combinations, further simplifying the prediction model to enhance its interpretability and practicality.

2. Materials and Methods

2.1. Field Site and Crop Management

A comprehensive field campaign was undertaken to gather RGB and multispectral images using UAVs, along with ground-truth phenotypic metrics. The campaign was conducted at an experimental oilseed rape field situated at the agricultural research station in Hangzhou, China. Figure 1 illustrates the overall location of the experimental site and provides an overview of the image captured by the UAV remote sensing platform in the oilseed rape field at Zhejiang University. The experiment consisted of two sets of replicates. The original test field had 47 rows, within which 3 incomplete rows were removed. The area and line spacing of each line were 24.4 m $\times$ 1.4 m and 0.3 m, respectively. There were 10 sampling plots in each row, and each sampling plot had an area of 2.4 m × 1.4 m. Because of the protection lanes, there were about 420 plots in total. Various nitrogen (N) fertilizer treatments were administered across all plots, ranging from N0 to N3 (0, 75, 150, and 225 kg/hm^2). Additionally, all subplots received consistent amounts of phosphorus (P) (60 kg/hm^2) and potassium (K) (150 kg/hm^2). The N fertilizers were applied in two stages, with 60% in mid-December and the remaining 40% in mid-February. On the contrary, phosphate and potash fertilizers were administered as a single-base treatment. The prevailing cultivar for the majority of subplots was ZD630.

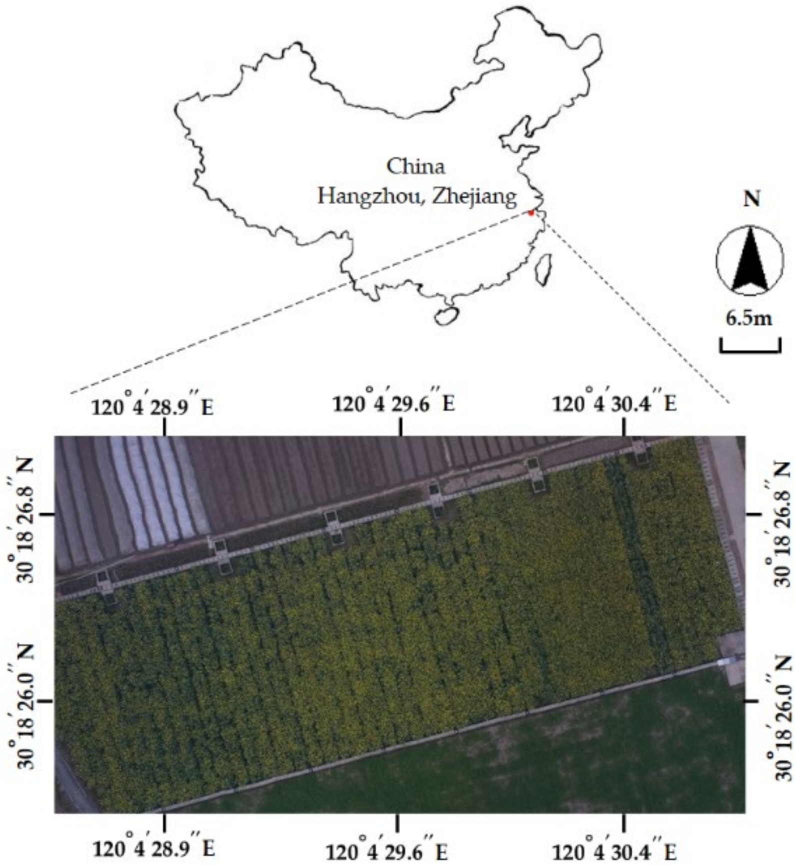

Figure 1. The general location of the experimental site and an overview of the image obtained by an unmanned aerial vehicle (UAV) remote sensing platform for the oilseed rape field at Zhejiang University.

The data collection and processing workflow of the inorganic remote sensing system is illustrated in Figure 2. The process can be broadly divided into the following steps. Firstly, RGB images and multispectral images (MSs) of winter oilseed rape at the pod-filling stage were collected in agricultural fields by using a drone equipped with RGB and multispectral cameras. This was followed by preprocessing steps, including radiometric correction, geometric correction, noise removal, and image stitching. Subsequently, features such as effective wavelengths and vegetation indices were extracted. Modeling and analysis were then conducted using methods such as ELM, BPNN and PLSR. Based on the above methodology, we evaluated the relationships between the selected EWs, VIs, and oilseed rape yield, thereby verifying the feasibility of yield estimation through the model. Finally, the model was validated against actual yield data, and yield enhancement suggestions were made while continuously optimizing the model to improve prediction accuracy and application effectiveness.

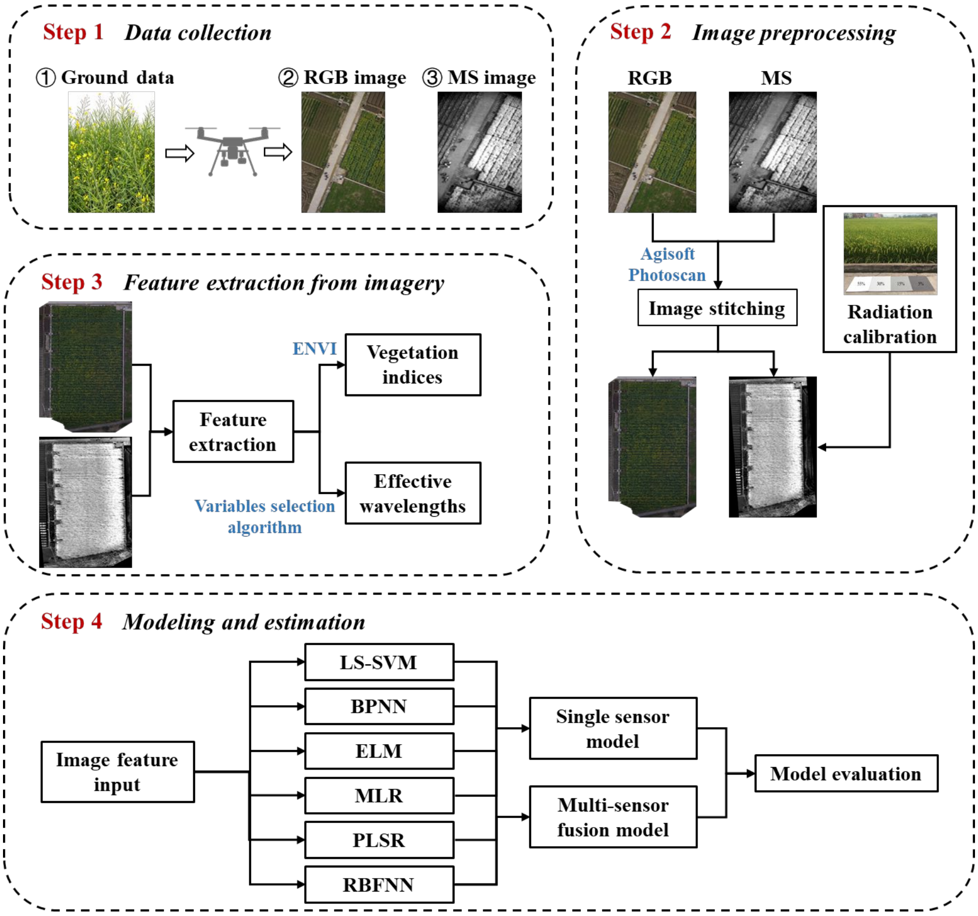

Figure 2. Research technology flowchart.

2.2. Data Acquisition

Upon the maturity of the oilseed rape, harvesting of all oilseed rape plots took place in May. Each plot underwent destructive measurements of the final yield, where above-ground plant materials were cut and placed in seed net bags. Subsequently, the collected materials were dried, and the actual yield of the sample plot was precisely measured. After sun exposure for 10 days for seed threshing, the seeds underwent cleaning and were placed in an oven at 60 °C until their weight stabilized (approximately 4 days). Subsequently, the total weight of all dried seeds was measured, and the plot yield was computed as the ratio of this cumulative weight to the ground area (kg/hm^2). Due to human factors, the yields of some plots in the measurement and production process were missing, leading to 373 effective plots for data analysis.

The UAV-based platform with an RGB camera (NEX-7, Sony, Tokyo, Japan) and multispectral imaging system (CMV2K; IMEC, Inc., Leuven, Belgium) was developed by Zhejiang University, as shown in Figure 3. The image sensors were carried by a lightweight and portable eight-rotor UAV, which employed advanced lithium-ion polymer batteries with a height of 0.35 m, a diameter of 1.1 m, a maximum takeoff weight of 8 kg, a maximum flight speed of 75 km/h, a flying height of up to 500 m, and a maximum flight time of 25 min under optimal weather conditions.

The drone platform includes an RGB camera with a spatial resolution of 6000 × 4000 pixels and a 25-band multispectral camera (679.15, 693.12, 718.58, 732.10, 745.14, 758.49, 771.28, 784.34, 796.27, 808.11, 827.03, 838.54, 849.10, 859.69, 870.74, 879.83, 889.10, 897.51.914.69, 922.27, 931.37, 936.54, 944.14, 950.60, and 955.72 nm). The multispectral camera consists of a multispectral imaging sensor, a lens, and a front optical filter, weighing a total of 123 g, with dimensions of 25.4 mm × 25.4 mm × 30.7 mm. The multispectral imaging sensor (IMEC, Leuven, Belgium) is a new type of snapshot imaging sensor (packaged hyperspectral mosaic snapshot imager) that features a resolution of 409 × 216 and an output frame rate of 42 fps, capable of capturing 25 narrow-band multispectral images (600–1000 nm) within 1/340 s.

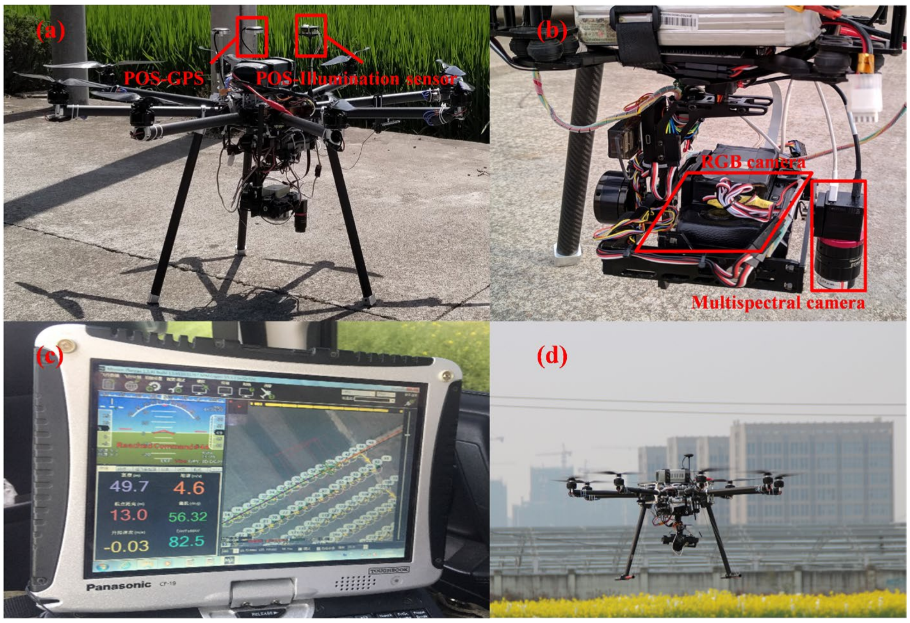

Figure 3. The UAV platform and integrated sensors: (**a**) POS system; (**b**) RGB and multispectral imaging sensors; (**c**) ground control system; (**d**) flight of the UAV system.

The platform was equipped with a POS system providing illumination information, a three-axis brushless head, radiometric calibration, and an image transmission system. The platform can realize the zero-delay high-definition back-transmission of images, radiation correction, and the geometric correction of remote sensing images. Flight campaigns were conducted during the pod filling stage between 2:00 and 4:00 pm, maintaining a flight attitude and speed of 50 m and 3 m/s, respectively. Weather conditions were optimal with clear skies, minimal cloud cover, and low wind speeds. The UAV platform software Mission Planner (ver. 1.3.74, ArduPilot Development Team, Ballarat, VIC, Australia) generated the flight route. To ensure effective image stitching, forward and side overlaps were set at 70% and 60%, respectively. To prevent anomalies in remote sensing images, the camera exposure time was adjusted based on brightness measurements obtained from an illuminometer (MQ-200, Apogee Instruments, Logan, UT, USA).

2.3. Image Preprocessing

Image stitching is the key technology for remote sensing image processing. Because the obtained single RGB image or multispectral image from the UAV-based platform has a small coverage and a large number of images, it is indispensable to splicing a plurality of images with a certain degree of overlap into a complete remote sensing image. Herein, full-spliced RGB and multispectral images were acquired by image stitching software Agisoft Photoscan (ver. 1.2.6, AgiSoft LLC, St. Petersburg, Russia) with rich point cloud information. The process mainly included the following steps: add photos, align photos, build dense cloud, build meshes and textures, and build and export orthomosaic. The quality of the point cloud was set to the highest to ensure the image maintained sufficient spatial resolution, which facilitated subsequent image processing. For each UAV flight operation, Agisoft Photoscan was used to quickly splice the original image data obtained. When it was found that the image stitching quality was poor or the stitching was not successful, the flight plan would be adjusted according to the condition of the UAV. Figure 4 shows a multispectral orthophoto image (at the wavelength of 889 nm) of the oilseed rape field with a low altitude of 50 m using Agisoft Photoscan.

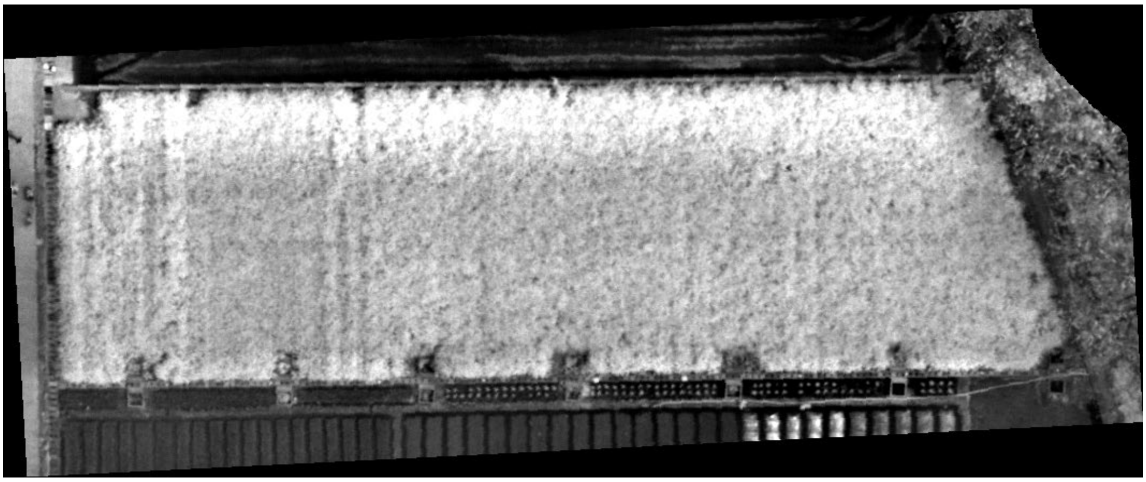

Figure 4. The stitching grayscale image of the multispectral image at 889 nm by Agisoft Photoscan.

2.4. Radiation Calibration

Radiation calibration was performed using four grayscale targets with a reflectance of 5%, 15%, 30%, and 55%, each measuring 0.6 m × 0.6 m × 1.2 cm. The spectral reflectance curve of the grayscale targets was acquired with a marine optical portable spectrometer (QE65000, Ocean Optics, Dunedin, FL, USA) while the drone was operating. The QE65000 has a spectral range of 350–1025 nm and a sampling interval of 1.377 nm. The average reflectance spectral data of the canopy of the oilseed rape under different nitrogen gradients were obtained by the calculation formula of the radiation calibration coefficient (Equation (1)):

$$R_i = k_i \times DN_i + b_i (i = 1, \cdots, 25) \tag{1}$$

where R_i is the reflectivity measured on the ground of four gradient grayscale targets, DN_i is the DN value of the target multispectral image obtained by the UAV remote sensing system, the gain, k_i, is the slope parameter of the linear equation, and the offset b_i is a linear regression intercept parameter, which is expressed around the radiation response introduced by the environment. According to the principle that the sum of squared residuals of the least squares algorithm is the smallest, the radiometric scaling coefficients k_i and b_i corresponding to the i-th band were obtained. Finally, the radiometric calibration coefficients (k and b) calculated by the grayscale targets were applied to the multispectral remote sensing image of oilseed rape, and the spectral reflectance data were calculated.

2.5. Feature Extraction from Imagery

A variety of vegetation indices were extracted from orthorectified RGB and multispectral images (Table 1). The color vegetation index is the visible light vegetation index, highlighting a special color, such as the green color of plants, which is a relatively intuitive feeling for humans. Vegetation indices obtained from RGB cameras are especially sensitive to the greenness of plants. These indices have been employed to extract green vegetation and calculate vegetation coverage, identify crop growth periods [28], estimate LAI, biomass [29], and chlorophyll content [30], and identify weeds [31], such as VDVI, NGRDI, VARI, GRRI, VEG, etc. Some improved vegetation indices such as ExGR, the Woebbecke index, and several combined vegetation indices were also used to explore the feasibility of predicting yield. These color vegetation indices have been widely cited and used in recent research [32]. Due to the band limitation of multispectral cameras, the multispectral narrow-band vegetation indices used in this study were mainly SRI, DVI, NDVI, SAVI, and several modified vegetation indices (OSAVI, MSAVI, EVI2, RDVI, and MSR). The technique known as the first derivative transformation is used to reduce background signals or noise and distinguish overlapping spectral features. Additionally, it effectively improves the correlation between spectral data and target parameters. In this sense, NDSI and RSI were computed based on the first derivative spectrum for yield estimation.

Table 1. List of vegetation indices (VIs) extracted from RGB and multispectral images.

Vegetation Indices	Formula	References
	RGB camera—Color Vis	
visible-band difference vegetation index, VDVI	$VDVI = (2G - R - B)/(2G + R + B)$	[30]
visible atmospherically resistant index, VARI	$VARI = (G - R)/(G + R - B)$	[33]
normalized green–red difference index, NGRDI	$NGRDI = (G - R)/(G + R)$	[28,34]
normalized green–blue difference index, NGBDI	$NGBDI = (G - B)/(G + B)$	[35]
red–green ratio index, RGRI	$RGRI = R/G$	[36]
green–red ratio index, GRRI	$GRRI = G/R$	[35]
modified green–red vegetation index, MGRVI	$MGRVI = \left(G^2 - R^2\right)/\left(G^2 + R^2\right)$	[37]
excess green index, ExG	$ExG = 2G - R - B$	[31]
color index of vegetation, CIVE	$CIVE = 0.441R - 0.881G + 0.385B + 18.78745$	[38]
vegetation, VEG	$VEG = G/\left(R^a \times B^{(1-a)}\right), a = 0.667$	[39]
excess green minus excess red, ExGR	$ExGR = ExG - ExR = ExG - 1.4R - G$	[40]
Woebbecke index, WI	$WI = (G - B)/(R - G)$	[31]
combination, COM	$COM = 0.25ExG + 0.3ExGR + 0.33CIVE + 0.12VEG$	[41]
combination 2, COM2	$COM2 = 0.36ExG + 0.47CIVE + 0.17VEG$	[42]
	Multispectral camera-- narrow band VIs	
simple ratio index, SRI	$SRI = R_{\lambda 1}/R_{\lambda 2}$	[43]
normalized difference vegetation index, NDVI	$NDVI = (R_{\lambda 1} - R_{\lambda 2})/(R_{\lambda 1} + R_{\lambda 2})$	[44]
enhanced vegetation index, EVI2	$EVI2 = 2.5 \times (R_{\lambda 1} - R_{\lambda 2})/(1 + R_{\lambda 1} + 2.4R_{\lambda 2})$	[45]
optimized soil-adjusted vegetation index, OSAVI	$OSAVI = 1.16 \times (R_{\lambda 1} - R_{\lambda 2})/(R_{\lambda 1} + R_{\lambda 2} + 0.16)$	[46]
soil-adjusted vegetation index, SAVI	$SAVI = 1.5 \times (R_{\lambda 1} - R_{\lambda 2})/(R_{\lambda 1} + R_{\lambda 2} + 0.5)$	[47]
difference vegetation index, DVI	$DVI = R_{\lambda 1} - R_{\lambda 2}$	[43]
renormalized difference vegetation index, RDVI	$RDVI = (R_{\lambda 1} - R_{\lambda 2})/\sqrt{(R_{\lambda 1} + R_{\lambda 2})}$	[48]
modified simple ratio, MSR	$MSR = \frac{R_{\lambda 1}/R_{\lambda 2} - 1}{\left(\sqrt{R_{\lambda 1}/R_{\lambda 2}} - 1\right)}$	[49]
modified soil-adjusted vegetation index, MSAVI	$MSAVI = 0.5 \times \left(2R_{\lambda 1} + 1 - \sqrt{(2R_{\lambda 1} + 1)^2 - 8 \times (R_{\lambda 1} - R_{\lambda 2})}\right)$	[50]
normalized difference spectral index, $NDSI_{(D_{\lambda 1}, D_{\lambda 2})}$	$NDSI_{(D_{\lambda 1}, D_{\lambda 2})} = (D_{\lambda 1} - D_{\lambda 2})/(D_{\lambda 1} + D_{\lambda 2})$	[51]
ratio vegetation index, $RSI_{(D_{\lambda 1}, D_{\lambda 2})}$	$RSI_{(D_{\lambda 1}, D_{\lambda 2})} = D_{\lambda 1}/D_{\lambda 2}$	[51,52]

Note: R, G, and B denote the radiometric normalized pixel values of each orthomosaic image's red, green, and blue band, respectively. $R_{\lambda 1}$ and $R_{\lambda 2}$ represent the reflectance of a variable band in the spectral range of 600–1000 nm. $D_{\lambda 1}$ and $D_{\lambda 2}$ are the first derivative values at λ_1 and λ_2 nm over the whole spectra. PLSR can effectively deal with multiple collinear problems and establish a linear regression model.

2.6. Machine Learning Algorithms

Machine learning algorithms are increasingly used in precision agriculture and UAV low-altitude remote sensing [53,54], especially for image segmentation, feature classification, and phenotypic information prediction. In this study, six machine learning algorithms were employed, i.e., MLR, PLSR, least squares support vector machine (LS-SVM), back propagation neural network (BPNN), extreme learning machine (ELM), and radial basis function neural network (RBFNN).

MLR is simple and easy to explain, and establishes the relationship between the spectrum and the measured index in the form of a linear equation [55]. That is, the procedure builds a model between the output variable Y (phenotypic information such as physiological and biochemical indices) and the input variable X (spectral data).

PLS simultaneously decomposes the spectral data (X-matrix, $N_{samples} \times K_{wavelengths}$) and the physical or chemical indicators (Y-matrix, $N_{samples} \times 1$) obtained from traditional measurements, aiming to optimize the covariance between Y and the linear combination of X [56]. PLSR transforms the original variables into mutually orthogonal dimensions, generating principal components or factors referred to as latent variables (LVs). These LVs encapsulate maximum information and covariance between spectral data and index values. Typically, leave-one-out cross-validation was utilized on the calibration set to ascertain the optimal number of LVs.

LS-SVM is derived from a standard support vector machine but employs a set of linear equations instead of quadratic programming problems to identify the support vectors. Furthermore, LS-SVM diverges from the empirical risk minimization principle typical in traditional neural networks, instead favoring the structural risk minimization principle to counteract overfitting [57]. In contrast to conventional chemometric approaches, increasing research indicates that LS-SVM effectively tackles both linear and nonlinear multivariate analysis issues [58–60]. BPNN primarily utilizes the error backpropagation algorithm to adjust the network connection weights after each training period. This process continues until the error between the actual output and the predicted output is minimized [61]. When the input set is determined, BPNN needs to set the number of hidden layers and nodes, learning algorithm and rate, transfer function, and training termination conditions. The neuron transfer function of BPNN generally includes threshold function, linear function and Sigmoid function. The implementation steps of BPNN can be found in the literature [62].

ELM is widely used in various classification and regression problems. ELM exhibits robust generalization capabilities within feedforward neural networks, utilizing a single-layer architecture. This approach involves randomly selecting input weights and biases for the hidden layer, effectively addressing challenges such as overfitting and local minima [63]. Furthermore, ELM achieves an optimal solution known for its fast learning and strong generalization. The algorithm's steps involve (1) randomly generating input weights and biases for hidden layer neurons, (2) computing the hidden layer's output matrix, and (3) determining the output weights. To achieve the optimal ELM model, the number of hidden layer nodes was fine-tuned incrementally.

RBFNN is a three-layer feedforward neural network comprising an input layer, a hidden layer, and an output layer [64]. RBFNN is a widely used machine learning algorithm with many advantages such as arbitrary approximation, strong generalization ability, fast training speed, and easy implementation. RBFNN uses RBF as the activation function. However, RBFNN has poor interpretability and requires massive training data. The optimization process may have data ill-conditioned phenomena when applying RBFNN. At present, based on the basic RBFNN algorithm, different improvements can be made and the appropriate algorithm can be selected according to need.

2.7. Variables Selection Algorithm

Genetic algorithm–partial least squares (GA-PLS) is a proficient variable selection technique introduced by Leardi [65], combining the advantages of the GA algorithm and PLS algorithm. GA-PLS is good at global searching and is not constrained by the restrictive assumptions of search space. It enables us to find the global optimal solution from discrete, multi-extreme, and noisy high-dimensional problems with great probability. The GA-PLS method selects sensitive wavelengths and optimizes the number of evaluations per run using the PLS algorithm. It aims to minimize cross-validation RMSECV or variance as fitness criteria. Additionally, GA-PLS determines the final subset frequency using a weighted average of frequencies. Increasing iterations and reducing selected variables enhance GA-PLS stability. In this study, 500 iterations were set to improve stability and accuracy. Recorded variables and their weighted frequencies across 500 runs were analyzed.

2.8. Model Evaluation

For the quantitative analysis models, we primarily utilized the correlation coefficient (R) and root mean square error (RMSE) to assess the model performances. The R is mainly used to measure the fitting effect of the model. An R-value closer to 1 usually indicates better fitting performance. The RMSE is used to calculate the standard deviation of the reference value and the model prediction value. It measures the prediction error of the model; therefore, a smaller RMSE value close to 0 is desirable. The stronger predictive ability of the model can be represented by a higher R of calibration (R_{cal}) and prediction (R_{pre}), and a lower RMSE of calibration (RMSEC) and prediction (RMSEP). Below are the definitions of the statistical parameters used:

$$R = \frac{\sum_{i=1}^{N} (\hat{y}_i - \overline{\hat{y}})(y_i - \overline{y})}{\sqrt{\sum_{i=1}^{N} (\hat{y}_i - \overline{\hat{y}})^2 (y_i - \overline{y})^2}} \tag{2}$$

$$RMSE = \sqrt{\frac{1}{N-1} \cdot \sum_{i=1}^{N} (y_i - \hat{y}_i)^2} \quad (3)$$

where y_i is the actual value, $\hat{y}_i$ is the predicted value of the yield in sample number i, and N is the number of spectra (samples).

The spectral data were extracted using ENVI 4.6 (ITT, Visual Information Solutions, Boulder, CO, USA). Statistical analyses, including one-way analysis of variance and correlation analysis, were carried out using SPSS (ver. 21.0, IBM-SPSS Inc., Chicago, IL, USA). Computation and implementation of machine learning algorithms were facilitated by Unscrambler X (ver. 10.1, CAMO AS, Oslo, Norway) and Matlab (ver. R2014b, The MathWorks, Natick, MA, USA) for chemometric analysis.

3. Results

3.1. Descriptive Statistics of Measured Yield

The statistical analysis based on the measured yield of oilseed rape under different nitrogen gradients is shown in Table 2. The yield range of 373 samples spanned from 2217.3 to 3586.3 kg/hm^2. The samples were randomly divided into calibration (248 samples) and prediction sets (125 samples) at a 2:1 ratio. The calibration set was used to develop the prediction model, while the prediction set was used to evaluate its performance. It can be seen from Table 2 that under different nitrogen fertilizer gradients, the yields of different sampling plots have obvious differences, and the sample sets (the calibration set and prediction set) cover a similar range of yield values, which is conducive to the establishment of stable quantitatively prediction models.

Table 2. Statistics of measured yield values of oilseed rape under different nitrogen gradients by standard methods.

Sample Sets	Number	Minimum (kg/hm^2)	Maximum (kg/hm^2)	Mean (kg/hm^2)	Standard Deviation (SD)
Calibration set	248	2217.30	3586.30	2942.68	274.23
Prediction set	125	2217.30	3526.80	2947.24	292.97

3.2. Characteristics of Spectral Profiles

Figure 5 illustrates the average reflectance spectra and standard deviation of the oilseed rape canopy across various nitrogen treatments based on the 25-band UAV multispectral imaging system. The band range is 679–956 nm. It can be seen that the average spectral change trend of the canopy with different nitrogen gradients was consistent. At 680–760 nm, the reflectivity increased sharply with wavelength and maintained a high reflectance between 760 and 900 nm. At 900–950 nm, the reflectance gradually decreased. Although the location and size of peaks and valleys were specific, the overall trend was similar to the spectral curve of other green plants such as tobacco [66], maize [67], and tomato [68]. The main peaks were located at 859.69 nm, 922.27 nm, and 944.14 nm, while the main troughs were found at 771.28 nm, 796.27 nm, and 936.54 nm. According to Weber et al. [67] and Zhang et al. [69], crop reflectance primarily correlates with photosynthetic capacity (495–680 nm), the red edge (680–780 nm), and plant water status (970 nm). Therefore, the peaks and troughs could be related to the pigment content and water status of oilseed rape and the red edge effect. There were obvious differences between different nitrogen gradients, especially in the range of 750–900 nm. The reflectance of the spectral curve with a high-nitrogen application rate in this range was higher than that with low-nitrogen fertilizer. The differences may be related to the effects of canopy structure, pods (intercellular spaces, cell alignment), leaf dip, leaf area index, biomass [70], and water status since the pod moisture content during the pod-filling period was high.

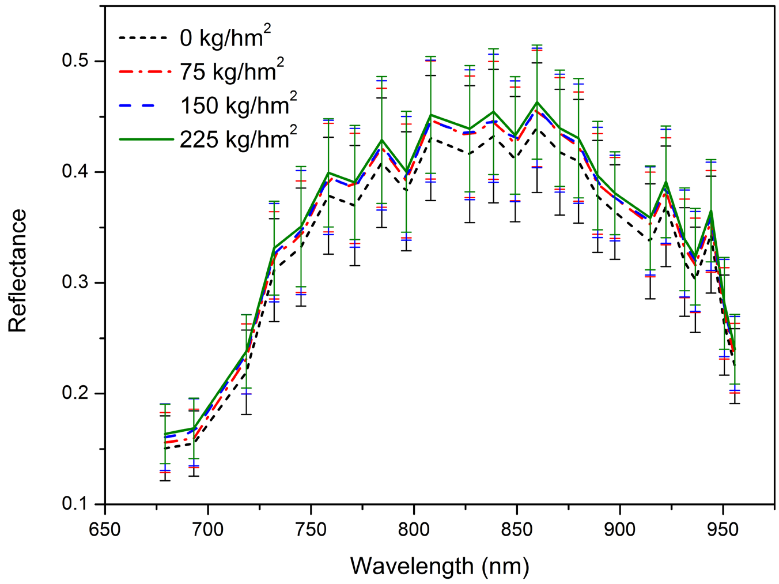

Figure 5. The average reflectance spectra and standard deviation (SD) of the oilseed rape canopy under different nitrogen treatments of '0 kg/hm^2', '75 kg/hm^2', '150 kg/hm^2', and '225 kg/hm^2' based on the UAV multispectral imaging system.

3.3. Yield Prediction with Full Spectra from the Multispectral Camera

Different machine learning algorithms are based on different principles. Regression analysis of data from different angles and selection of appropriate regression analysis models will be beneficial to realizing yield estimation. The full wavelengths from the 25-band multispectral camera were used as an input to establish regression models with various machine learning algorithms to predict the yield. The specific parameter settings and final results are shown in Table 3. The PLSR, MLR, LS-SVM, BPNN, ELM, and RBFNN models all had satisfactory performance, with R_{cal} and R_{pre} both greater than 0.78. The optimal prediction model was BPNN with R_{cal} and R_{pre} values of 0.8145 and 0.8232, respectively, and RMSEC and RMSEP values of 158.7 kg/hm^2 and 166.9 kg/hm^2, respectively. The LS-SVM and ELM models also achieved good results. The R_{pre} and RMSEP values of LS-SVM were 0.8005 and 176.3 kg/hm^2, respectively. The R_{pre} and RMSEP values of ELM were 0.8023 and 170.3 kg/hm^2, respectively. The above analysis showed that the nonlinear models (BPNN, LS-SVM, and ELM) were slightly better than the simple linear models (PLSR and MLR) based on multiple machine learning algorithms. The selection of advanced data mining algorithms was beneficial to improving the accuracy of estimation models.

Table 3. The results for yield prediction using different machine learning algorithms based on the full spectra of the UAV multispectral imaging system.

Machine Learning Algorithms	Full Spectra	Parameter [a]	Calibration		Prediction	
			R_{cal}	RMSEC	R_{pre}	RMSEP
PLSR	25	7	0.7920	167.2	0.7918	179.0
MLR	25	-	0.8144	160.0	0.7880	179.8
LS-SVM	25	$(4.7 \times 10^4, 6.8 \times 10^3)$	0.8212	156.2	0.8005	176.3
BPNN	25	4	0.8145	158.7	0.8232	166.9
ELM	25	27	0.8066	161.8	0.8023	170.3
RBFNN	25	85	0.8273	153.7	0.7750	184.5

[a] Parameters: number of LVs for partial least squares regression (PLSR), (γ, σ^2) for least squares support vector machine (LS-SVM), number of hidden neurons for extreme learning machine (ELM), and number of neurons in the hidden layer for back propagation neural network (BPNN) or radial basis function neural network (RBFNN). The RMSEC and the RMSEP values are both expressed in kilograms per hectare (kg/hm^2). The same applies below.

3.4. Narrow-Band VI Extraction from the Multispectral Camera

VI has been widely used to obtain and analyze crop phenotypic information. The RGB color VI contained a fixed band combination, while the multispectral narrow-band VI utilized all the bands in the 600–1000 nm spectra of the best VI applicable to yield estimation. In this study, we utilized Pearson correlation analysis, a widely employed method for assessing the correlation between variables. Initially, we computed Pearson correlation coefficients (r) between vegetation indices and in situ data. Subsequently, we identified indices that exhibited a relatively strong and statistically significant correlation for further modeling analysis [71]. The contour maps of the correlation coefficients (absolute values) between yield and narrow-band VIs (SRI, NDVI, EVI2, OSAVI, SAVI, DVI, RDVI, MSR, MSAVI, $NDSI_{(D\lambda1,\ D\lambda2)}$, and $RSI_{(D\lambda1,\ D\lambda2)}$) using the thorough combinations of two wavebands at λ1 and λ2 nm based on the UAV multispectral imaging system are plotted in Figure 6. The intersection point in the maps correspond to the absolute value of the r between the vegetation index calculated by the reflectance spectrum or the first derivative of each pair of bands and the yield. The color bar shows the value of r. A redder color corresponds to a larger r, and a bluer color represents a smaller r. From the correlation coefficient maps, the optimal band combination and the wavelength width for estimating the yield of oilseed rape can be obtained.

According to Figure 6, for the $MSAVI_{(R\lambda1,\ R\lambda2)}$, $RDVI_{(R\lambda1,\ R\lambda2)}$, $EVI2_{(R\lambda1,\ R\lambda2)}$ and $SAVI_{(R\lambda1,\ R\lambda2)}$, the best correlation of the band combination is at 944 nm and 808 nm. Additionally, the absolute values of the r were up to 0.5444, 0.5413, 0.5320, and 0.5233, respectively. The optimal band combination obtained by $DVI_{(R\lambda1,\ R\lambda2)}$, $OSAVI_{(R\lambda1,\ R\lambda2)}$, $SRI_{(R\lambda1,\ R\lambda2)}$, $MSR_{(R\lambda1,\ R\lambda2)}$, and $NDVI_{(R\lambda1,\ R\lambda2)}$ was 871 nm and 796 nm. The absolute values of the correlation coefficient were up to 0.4968, 0.4722, 0.4644, 0.4635, and 0.4625, respectively. For the $NDSI_{(D\lambda1,\ D\lambda2)}$ and $RSI_{(D\lambda1,\ D\lambda2)}$ of the first derivative spectrum, the best correlation of the bands was 937 nm and 732 nm, where the absolute values of the r were 0.5158 and 0.5115, respectively. Thus, based on these contour maps, the optimal VIs were available for $MSAVI_{(808,\ 944)}$, $RDVI_{(944,\ 808)}$, $EVI2_{(944,\ 808)}$, $SAVI_{(944,\ 808)}$, $DVI_{(871,\ 796)}$, $OSAVI_{(871,\ 796)}$, $SRI_{(871,\ 796)}$, $MSR_{(871,\ 796)}$, $NDVI_{(871,\ 796)}$, $RSI_{(D937,\ D732)}$, and $NDSI_{(D937,\ D732)}$. Based on the multispectral narrow-band VIs selected above, it is necessary to verify the correlation and perform the one-way variance test. Table 4 lists the absolute values of the r between the eleven narrow-band VIs and yields in descending order. It can be seen that the correlation coefficients varied between 0.463 and 0.544 ($p < 0.01$), indicating strong correlations between the yield of oilseed rape and UAV imagery-based VIs. The absolute values of all Pearson correlation coefficients were higher than 0.4, and the F-test value corresponding to the vegetation index with a large Pearson correlation coefficient was also larger. Therefore, the 11 preferred VIs for the above were all used for the input of the post-machine-learning algorithms.

Table 4. The correlation coefficient between canopy vegetation index and yield of oilseed rape based on multispectral images.

Vegetation Index	Pearson Correlation Coefficient	Significance	Vegetation Index	Pearson Correlation Coefficient	Significance
$MSAVI_{(808,\ 944)}$	0.544 **	0.000	$DVI_{(871,\ 796)}$	−0.497 **	0.000
$RDVI_{(944,\ 808)}$	0.541 **	0.000	$OSAVI_{(871,\ 796)}$	−0.472 **	0.000
$EVI2_{(944,\ 808)}$	−0.532 **	0.000	$SRI_{(871,\ 796)}$	−0.464 **	0.000
$SAVI_{(944,\ 808)}$	0.523 **	0.000	$MSR_{(871,\ 796)}$	−0.464 **	0.000
$RSI_{(D937,\ D732)}$	−0.516 **	0.000	$NDVI_{(871,\ 796)}$	−0.463 **	0.000
$NDSI_{(D937,\ D732)}$	−0.511 **	0.000			

Note: ** indicates significance at the 0.01 alpha level.

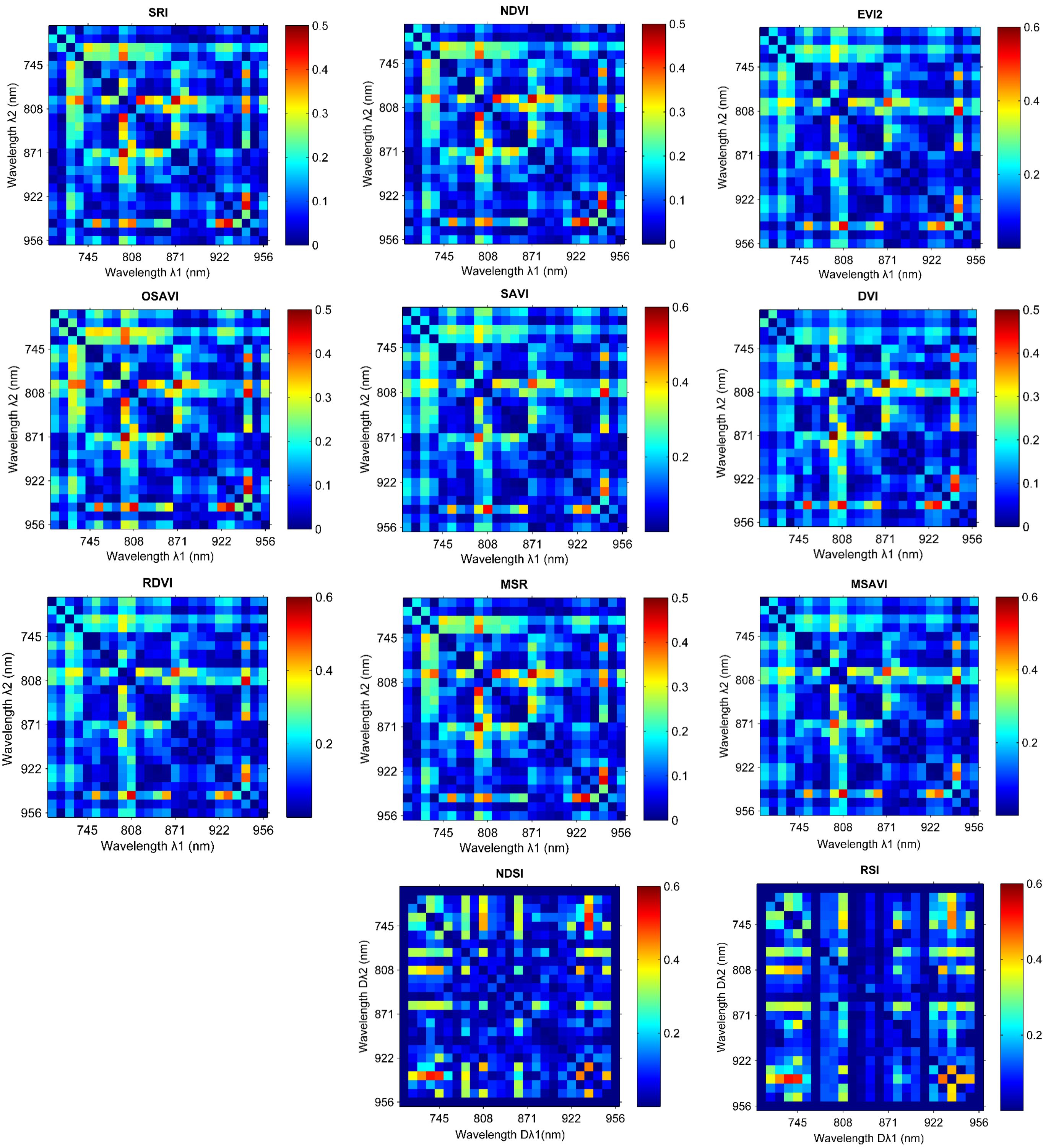

Figure 6. Contour maps of the correlation coefficients between yield and narrow-band vegetation indices using the thorough combinations of two wavebands at λ1 and λ2 nm based on the UAV multispectral imaging system.

3.5. Color VI Extraction from the RGB Camera

Table 5 compiles the associations between oilseed phenotypic traits (yield) and remote sensing indices derived from RGB imagery. Pearson coefficients (r) were calculated using IBM SPSS software, version 29.0.2. Notably, 12 color VIs exhibited an absolute r greater than 0.5 ($p < 0.01$, n = 373), signifying robust correlations between field measurement data and

UAV imagery-based indices. Furthermore, one-way analysis of variance was performed on VIs and yield to ensure that the preferred VIs also had a higher *F* test value. At the statistical significance level of sig = 0.05, the results of one-way ANOVA are shown in Table 6. The results of VI ranking based on correlation analysis and one-way ANOVA were not completely consistent, but the ranking results were similar. A large correlation coefficient corresponded to a large *F* value. Based on the results of correlation analysis and one-way ANOVA, and considering the simplification of the later model, the first 12 color vegetation indices ($|r| > 0.5$) were selected as the input of the later machine learning models, namely CIVE, VEG, GRRI, VDVI, NGRDI, MGRVI, RGRI, VARI, COM2, NGBDI, ExG, and ExGR. Among them, CIVE had the highest correlation with $r = 0.626$. Most of the color VIs were positively correlated with the yield of oilseed rape.

Table 5. The correlation coefficient between the canopy vegetation index and yield of oilseed rape based on the RGB camera.

Vegetation Index	Pearson Correlation Coefficient	Significance	Vegetation Index	Pearson Correlation Coefficient	Significance
CIVE	−0.626 **	0.000	VARI	0.611 **	0.000
VEG	0.614 **	0.000	COM2	0.609 **	0.000
GRRI	0.613 **	0.000	NGBDI	0.603 **	0.000
VDVI	0.612 **	0.000	ExG	0.599 **	0.000
NGRDI	0.612 **	0.000	ExGR	−0.582 **	0.000
MGRVI	0.612 **	0.000	COM	−0.257 **	0.000
RGRI	−0.611 **	0.000	WI	−0.024	0.646

Note: ** indicates significance at the 0.01 alpha level.

Table 6. The results of ANOVA using vegetation indices based on the RGB camera.

Vegetation Index	*F* Value	Significance	Vegetation Index	*F* Value	Significance
RGRI	2.836	0.000	VDVI	2.647	0.000
VARI	2.821	0.000	COM2	2.613	0.000
NGRDI	2.818	0.000	ExGR	2.577	0.000
MGRVI	2.817	0.000	NGBDI	2.378	0.000
GRRI	2.799	0.000	ExG	2.339	0.000
VEG	2.704	0.000	COM	1.226	0.101
CIVE	2.690	0.000	WI	0.127	1.000

3.6. Yield Prediction with VIs Using Machine Learning Algorithms

The stability of the estimation models based on a single vegetation index could have been affected by the presence of fewer features. Compared with univariate analysis, multivariate analysis can effectively reduce the impact of samples and fluctuations between points and can extract effective information for modeling. Therefore, based on the above-mentioned preferred vegetation index combinations as inputs, quantitative prediction models were established by different machine learning algorithms (PLSR, MLR, LS-SVM, BPNN, ELM, and RBFNN), and the parameter settings were as described. Table 7 shows the prediction results of yield based on the multispectral vegetation index, RGB and multi-spectral VI fusion with different machine learning algorithms.

It can be seen from the table that the PLSR, MLR, LS-SVM, BPNN, ELM, and RBFNN models have good prediction results based on the regression analysis models established by the 11 VIs of the multispectral camera, while R_{cal} and R_{pre} are both greater than 0.70. The LS-SVM and BPNN models were superior to the others; R_{pre} and RMSEP of LS-SVM were 0.7502 and 193.2 kg/hm^2, respectively. BPNN performed the best according to the comprehensive results; the R_{pre} and RMSEP values were 0.7655 and 188.3 kg/hm^2, respectively. Meanwhile, we attempted to establish regression analysis models with all color VIs. The correlation coefficients for both the calibration set and the prediction set hovered around 0.7, suggesting a constrained contribution of RGB cameras to yield estimation. Consequently, the main comparison of this study was between the multispectral camera and dual sensors. Based on the quantitative models established by the fusion of VIs from the multispectral camera and RGB camera, PLSR, MLR, LS-SVM, BPNN, ELM, and RBFNN all achieved promising prediction results, where R_{pre} was greater than 0.75. Moreover, the R_{cal} and R_{pre} values of BPNN, ELM, and RBFNN were all greater than 0.80, especially for the ELM and RBFNN estimation models. RBFNN performed best with the R_{pre} and RMSEP being 0.8143 and 171.9 kg/hm^2, respectively. Overall, the regression models based on the VIs of UAV-based dual sensors were better than those only using narrow-band VIs.

Therefore, multi-sensor fusion in UAV systems should be suggested for crop phenotypic information analysis.

Table 7. The combination of vegetation indices for yield prediction by different machine learning algorithms based on the RGB and multispectral imaging system.

Camera Sensor Type	Vegetation Indices	Machine Learning Algorithms	EWs	Parameter [a]	Calibration		Prediction	
					R_{cal}	RMSEC	R_{pre}	RMSEP
Multispectral camera	MSAVI$_{(808, 944)}$, RDVI$_{(944, 808)}$, EVI2$_{(944, 808)}$, SAVI$_{(944, 808)}$, DVI$_{(871, 796)}$, OSAVI$_{(871, 796)}$, SRI$_{(871, 796)}$, MSR$_{(871, 796)}$, NDVI$_{(871, 796)}$, RSI$_{(D937, D732)}$, NDSI$_{(D937, D732)}$	PLSR	11	6	0.7075	193.5	0.7166	204.1
		MLR	11	-	0.7216	189.4	0.7220	202.2
		LS-SVM	11	(4.2, 22.4)	0.7732	173.6	0.7502	193.2
		BPNN	11	6	0.7603	177.8	0.7655	188.3
		ELM	11	17	0.7270	188.2	0.7149	204.5
		RBFNN	11	103	0.7298	187.9	0.7110	205.6
Multispectral camera, RGB camera	CIVE, VEG, GRRI, VDVI, NGRDI, MGRVI, RGRI, VARI, COM2, NGBDI, ExG, ExGR; MSAVI$_{(808, 944)}$, RDVI$_{(944, 808)}$, EVI2$_{(944, 808)}$, SAVI$_{(944, 808)}$, DVI$_{(871, 796)}$, OSAVI$_{(871, 796)}$, SRI$_{(871, 796)}$, MSR$_{(871, 796)}$, NDVI$_{(871, 796)}$, RSI$_{(D937, D732)}$, NDSI$_{(D937, D732)}$	PLSR	23	4	0.7211	189.6	0.7751	184.5
		MLR	23	-	0.7808	171.0	0.7690	187.0
		LS-SVM	23	(3.6×10^7, 3.8×10^6)	0.7937	166.7	0.7582	190.3
		BPNN	23	6	0.8013	163.9	0.8080	173.3
		ELM	23	71	0.8033	163.0	0.8153	171.0
		RBFNN	23	18	0.8137	159.1	0.8143	171.9

[a] Parameters and abbreviations are the same as in Table 3.

3.7. Variable Selection and Model Simplification Based on GA-PLS

Excessive VIs or wavelengths are prone to multiple collinearity and overfitting problems. In order to further simplify the prediction models, the 25 bands based on the multispectral camera and the 23 VIs based on the fusion of the multispectral camera and the RGB camera were selected by the genetic algorithm. Prioritizing the significance of variables is essential for variable selection and model simplification. GA-PLS achieves this by sorting the importance of variables according to their selection frequency. As illustrated in Figure 7, Figure 7a depicts the frequency distribution of the selected wavelengths. The automatically generated frequency map had two horizontal lines, which represented different variables' modeling. The model with 18 variables was superior, so the effective wavelengths depended on the selected frequency size and importance: 950.6, 870.7, 808.1, 859.7, 796.3, 944.1, 879.8, 936.5, 827.0, 784.3, 849.1, 838.5, 955.7, 888.1, 693.1, 897.5, 914.7, 718.6 nm. It was indicated that the above 18 variables were dominant in the yield estimation of oilseed rape. Similarly, Figure 7b indicates the frequency of the selected VIs, and the lower horizontal line indicates that the selected characteristic VI number was 9, according to the selected frequency size and importance, including RDVI$_{(944, 808)}$, EVI2$_{(944, 808)}$, OSAVI$_{(871, 796)}$, DVI$_{(871, 796)}$, SAVI$_{(944, 808)}$, NGRDI, NGBDI, ExG, and VDVI.

Different machine learning algorithms were compared with fewer variables (EWs or VIs) selected by GA-PLS. The results are shown in Table 8. Regression models (PLSR, MLR, LS-SVM, BPNN, ELM, and RBFNN) based on 18 EWs achieved satisfactory prediction results, with R_{cal} and R_{pre} values greater than 0.78. In particular, the estimated models of BPNN and ELM outperformed the others. Among them, BPNN manifested the best performance, for which R_{pre} and RMSEP were 0.8114 and 172.6 kg/hm^2, respectively.

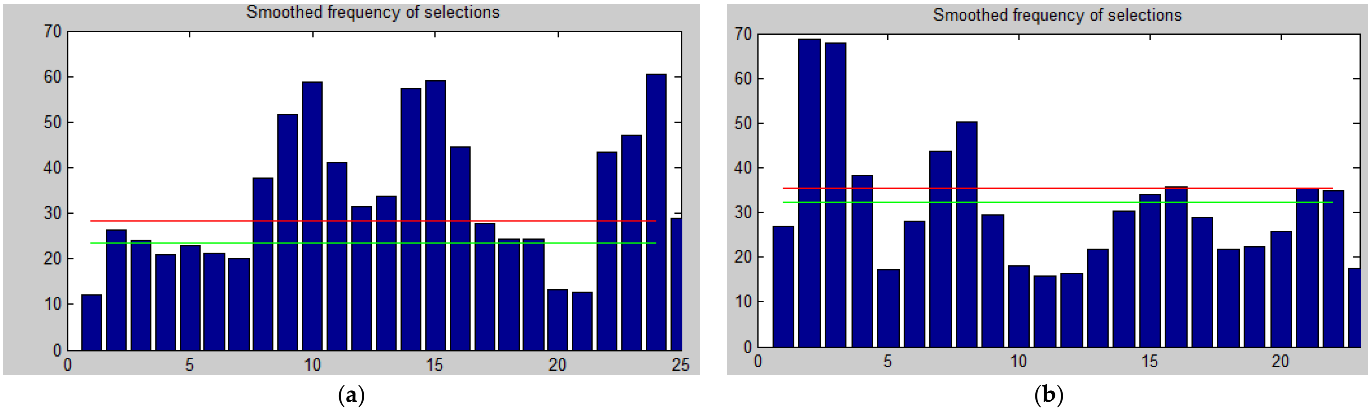

Figure 7. Selection of effective features by genetic algorithm–partial least squares according to smoothed frequency of selections: (**a**) wavelengths; (**b**) vegetation indices.

Table 8. The effective features for yield prediction by different machine learning algorithms based on the RGB and multispectral imaging system.

Camera Sensor Type	Features of Variables	Machine Learning Algorithms	EWs/VIs	Parameter [a]	Calibration		Prediction	
					R_{cal}	RMSEC	R_{pre}	RMSEP
Multispectral camera	950.6, 870.7, 808.1, 859.7, 796.3, 944.1, 879.8, 936.5, 827.0, 784.3, 849.1, 838.5, 955.7, 888.1, 693.1, 897.5, 914.7, 718.6 (nm)	PLSR	18	7	0.7855	169.8	0.7851	180.9
		MLR	18	-	0.7903	167.7	0.7898	179.2
		LS-SVM	18	(4.8×10^4, 6.1×10^3)	0.8082	161.3	0.7995	176.8
		BPNN	18	4	0.8087	160.9	0.8114	172.6
		ELM	18	27	0.8052	162.3	0.8082	173.0
		RBFNN	18	67	0.8075	161.5	0.7984	177.0
Multispectral camera, RGB camera	$RDVI_{(944, 808)}$, $EVI2_{(944, 808)}$, $OSAVI_{(871, 796)}$, $DVI_{(871, 796)}$, $SAVI_{(944, 808)}$, NGRDI, NGBDI, ExG, VDVI	PLSR	9	4	0.7285	187.9	0.7767	183.9
		MLR	9	-	0.7536	180.0	0.7983	177.1
		LS-SVM	9	(2.2×10^6, 5.0×10^4)	0.7596	178.1	0.7870	180.9
		BPNN	9	4	0.7977	165.1	0.8113	173.4
		ELM	9	39	0.8125	159.6	0.8118	170.9
		RBFNN	9	3	0.8186	157.4	0.8002	175.2

[a] Parameters and abbreviations are the same as those in Table 3.

BPNN, ELM, and RBFNN models based on the nine selected VIs obtained promising prediction results, with R_{pre} being greater than 0.8. Moreover, the ELM model was preferable, for which R_{pre} and RMSEP were 0.8118 and 170.9 kg/hm^2, respectively. Compared with the models with full wavelengths, for all VIs, the performance of partial models based on selected variables was improved, indicating that sorting the importance of variables facilitated improvements in and simplification of the estimation models of yield. The optimal prediction models based on the full wavelengths, all the vegetation indices, selected EWs, and selected VIs are shown in Figure 8. Overall, the performance of the optimal estimation models based on effective variables was slightly inferior to that of the full wavelengths or all VIs; nonetheless, the number of wavelengths was reduced by 28%, and the number of vegetation indices was reduced by 61%. The selected variables reduced the operation time and facilitated speed in the process of establishing the models.

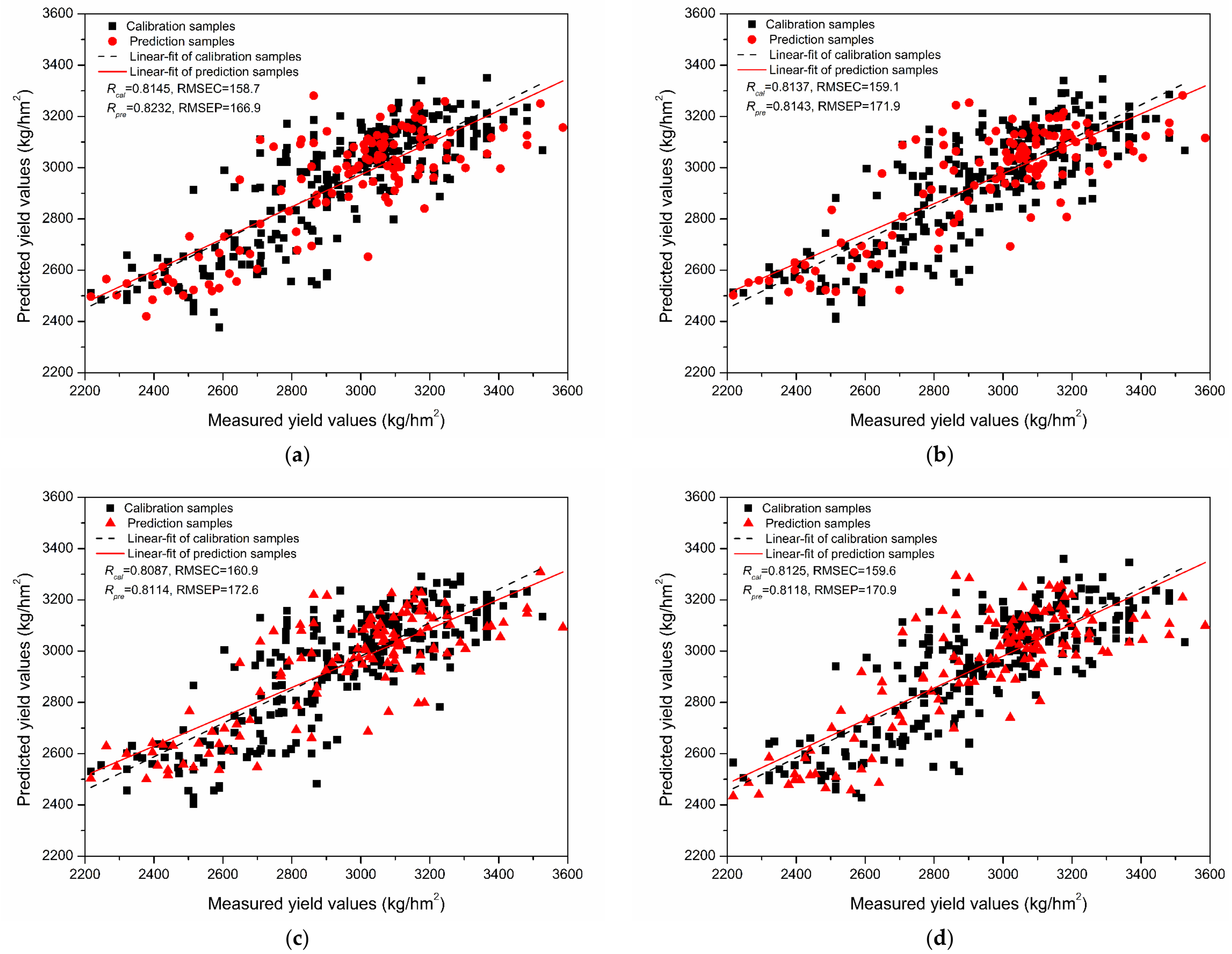

Figure 8. The scatter plot of predicted yield values vs. measured yield values: the optimal models with full wavelengths (**a**) and selected EWs (**c**) from the multispectral camera; the optimal models with all the vegetation indices (**b**) and selected VIs (**d**) from the dual cameras.

4. Discussion

In this study, we thoroughly examined the effectiveness of various VIs in predicting vegetation growth conditions, expanding the research scope compared to that of previous studies that relied solely on a single VI. Through one-way analysis of variance (ANOVA) and Pearson correlation analysis, we identified VIs that performed particularly well in predicting phenotypic information. This process not only improved the predictive accuracy and efficiency of the model but also provided high-quality data input for subsequent machine learning algorithms. Compared to traditional methods like MLR and PLSR, we introduced advanced machine learning algorithms such as BPNN, LS-SVM, ELM, and RBFNN. These algorithms excel in modeling nonlinear relationships, significantly improving the accuracy and robustness of the models (see Tables 3, 7 and 8).

Notably, the application of GA-PLS for optimizing VI combinations not only significantly increased computational speed but also further enhanced the predictive capabilities of the models. From the optimal VI combination selected by GA-PLS, we found that the first five variables were narrowband vegetation indices, while the last four were color vegetation indices. This selection strategy provided strong support for a deeper understanding of the multidimensional characteristics of crop growth. For instance, narrowband vegetation indices are closely related to physiological traits such as chlorophyll content and water status. However, color vegetation indices more intuitively reflect changes in canopy greenness [28,72]. These findings are consistent with those of previous research, such as the study by Zhang et al. [73], which highlighted the high sensitivity of color vegetation indices based on RGB images in detecting canopy temperature. Similarly, the work of Haboudane et al. [74] confirmed the significant role of multispectral narrowband VIs in reflecting crop physiological traits.

This study further validated the dominant role of multispectral cameras in yield prediction. Compared to using only RGB images, multispectral cameras can capture richer spectral information, thereby improving the accuracy of predictions. This is also reflected in the study by Ashapure et al. [75], where the introduction of multispectral data significantly enhanced the monitoring of crop growth conditions. Additionally, the inclusion of near-infrared spectral information was particularly beneficial for estimating biochemical traits, which is consistent with the findings of Zheng et al. [76]. Although RGB imagery offered advantages in agricultural monitoring due to its low cost and ease of acquisition, its limited spectral bands resulted in less comprehensive reflection of crop growth and physiological information [77]. Most previous studies have primarily relied on multispectral and hyperspectral imaging technologies to extract more detailed spectral features, which were closely related to crop physiological status and growth conditions. For instance, the NIR band was effective for estimating crop water content and chlorophyll levels, while the SWIR band aided in monitoring crop nutrient status [34]. In accordance with the objectives of this paper, we employed a UAV remote sensing system equipped with both RGB and multispectral cameras to capture more detailed spectral and image data of oilseed rape. This approach helped improve the accuracy of estimating oilseed rape growth status and yield, as demonstrated by Zheng, who enhanced the estimation of crop leaf nitrogen concentration through remote sensing techniques [76]. Using the RGB and multispectral data collected by the UAV system, we developed a series of robust predictive models such as the RBFNN and BPNN. These models exhibited excellent predictive performance and robustness when processing both RGB and multispectral data. Wan et al. [26] demonstrated that integrating multi-source data with advanced modeling algorithms greatly enhances the accuracy of monitoring crop growth conditions.

Notably, our study integrated a dual-sensor strategy combining RGB and multispectral imaging. This fusion not only compensated for the spectral limitations of solely using RGB imagery but also supplemented the spatial and temporal details of multispectral data through the high spatial resolution of RGB images. This multi-source data fusion method demonstrated broad prospects in agricultural applications. For example, Li et al. [78] showed that models combining RGB and multispectral data outperformed single models in crop disease detection and yield prediction. Further combinations of RGB and multispectral data demonstrate that dual-sensor fusion results can improve yield estimation and can also be extended to monitor growth-related characteristics in other field crops. This also underscores the need for utilizing the commercial RGB camera mounted on a drone for oilseed rape yield estimation. The UAV-based platform equipped with a RGB camera can significantly reduce equipment costs compared to multispectral cameras [79]. Additionally, RGB images with high spatial resolution can visually understand the dynamics of field crop growth, which has been reported in previous studies [80,81]. Therefore, the above studies demonstrated the feasibility of using micro-miniature UAV remote sensing systems based on RGB and 25-band multispectral images to predict yield, and the great potential of this UAV system to predict other high-throughput plant phenotypes and advanced breeding programs in precision agriculture. In addition, multi-sensor data fusion is critical for UAV applications and can significantly extend the phenotypic information analysis of sensors and platforms for more crops.

5. Conclusions

We demonstrated the feasibility and potential of using data fusion from UAV-based RGB and multispectral imagery with different machine learning algorithms to improve yield prediction. The key findings of this research are as follows: (1) Using spectral data collected during the pod filling stage of oilseed rape from the multispectral camera, we successfully developed high-accuracy and robust yield prediction models ($R_{pre} > 0.78$), confirming the feasibility of early yield forecasting in oilseed rape fields using low-altitude remote sensing technology. (2) Through systematic analysis and comparison of various VIs in yield estimation, we identified the optimal VIs for oilseed rape yield estimation and multi-source data fusion. The inclusion of these VIs significantly improved the performance of the prediction models ($R_{pre} > 0.81$). (3) Additionally, we found that the models based on a fusion of data (EWs, color VIs and narrowband VIs) from dual sensors not only improved yield prediction accuracy but also enhanced the reliability of the models in practical applications.

It was proven that the lightweight UAV equipped with RGB and multispectral cameras was advantageous in obtaining phenotypic information on oilseed rape. A technical route was proposed for the low-altitude remote sensing of UAV: image acquisition, image stitching and processing, effective wavelength or vegetation index selection, and the use linear and nonlinear prediction models using machine learning algorithms. For future research, it is of great importance and an urgent need to establish a universal model and a low-altitude UAV-based remote sensing database with more characteristics and phenotypic information related to the growth of oilseed rape in different varieties and different regions. It is important to ensure that the analytical accuracy of the model meets the needs of decision-making about oilseed rape breeding.

Author Contributions: Conceptualization, H.Z.; formal analysis, S.L. and C.L.; funding acquisition, H.Z.; methodology, H.Z.; project administration, H.Z.; supervision, H.Z., Y.H. and J.-L.X.; validation, H.Z., S.L. and C.L.; writing—original draft, H.Z.; writing—review and editing, H.Z., S.L., C.L., Y.H. and J.-L.X. All authors have read and agreed to the published version of the manuscript.

Funding: This work was supported by the Natural Science Foundation of Guangxi (No. 2024 GXNSFBA010381), the Guangxi Science and Technology Base and Talent Project (Guike AD21075018), and a grant (No. NCOC-24-02) from Key Laboratory of Nonlinear Circuit and Optical Communications (Guangxi Normal University), Education Department of Guangxi Zhuang Autonomous Region.

Data Availability Statement: Data will be made available from the corresponding author on reasonable request.

Acknowledgments: We would like to thank Wenxin Yin, Jiangpeng Zhu, Qishuai Zheng, Yijian Li, Liwen He, and Weikang Wu, who participated in the experiments.

Conflicts of Interest: The authors declare that they have no known competing interests.

References

1. Mia, M.S.; Tanabe, R.; Habibi, L.N.; Hashimoto, N.; Homma, K.; Maki, M.; Matsui, T.; Tanaka, T.S. Multimodal deep learning for rice yield prediction using UAV-based multispectral imagery and weather data. *Remote Sens.* **2023**, *15*, 2511. [CrossRef]
2. Su, C.; Hong, J.; Wang, J.; Yang, Y. Quick and Accurate Counting of Rapeseed Seedling with Improved YOLOv5s and Deep-Sort Method. *Phyton* **2023**, *92*, 2611. [CrossRef]
3. Natarajan, S.; Basnayake, J.; Wei, X.; Lakshmanan, P. High-throughput phenotyping of indirect traits for early-stage selection in sugarcane breeding. *Remote Sens.* **2019**, *11*, 2952. [CrossRef]
4. Guo, Y.; Zhang, X.; Chen, S.; Wang, H.; Jayavelu, S.; Cammarano, D.; Fu, Y. Integrated UAV-based multi-source data for predicting maize grain yield using machine learning approaches. *Remote Sens.* **2022**, *14*, 6290. [CrossRef]
5. Ahmed, S.; Nicholson, C.E.; Rutter, S.R.; Marshall, J.R.; Perry, J.J.; Dean, J.R. Use of an unmanned aerial vehicle for monitoring and prediction of oilseed rape crop performance. *PLoS ONE* **2023**, *18*, e0294184. [CrossRef]
6. Li, Y.; Yuan, N.; Luo, S.; Yang, K.; Fang, S.; Peng, Y.; Gong, Y. Abundance considerations for modeling yield of rapeseed at the flowering stage. *Front. Plant Sci.* **2023**, *14*, 1188216. [CrossRef]
7. Li, W.; Weiss, M.; Garric, B.; Champolivier, L.; Jiang, J.; Wu, W.; Baret, F. Mapping crop leaf area index and canopy chlorophyll content using UAV multispectral imagery: Impacts of illuminations and distribution of input variables. *Remote Sens.* **2023**, *15*, 1539. [CrossRef]
8. Yan, P.; Han, Q.; Feng, Y.; Kang, S. Estimating lai for cotton using multisource uav data and a modified universal model. *Remote Sens.* **2022**, *14*, 4272. [CrossRef]
9. Zhou, L.; Meng, R.; Yu, X.; Liao, Y.; Huang, Z.; Lü, Z.; Xu, B.; Yang, G.; Peng, S.; Xu, L. Improved yield prediction of ratoon rice using unmanned aerial vehicle-based multi-temporal feature method. *Rice Sci.* **2023**, *30*, 247–256.

10. Luo, S.; Jiang, X.; Jiao, W.; Yang, K.; Li, Y.; Fang, S. Remotely sensed prediction of rice yield at different growth durations using UAV multispectral imagery. *Agriculture* **2022**, *12*, 1447. [CrossRef]
11. Lukas, V.; Huňady, I.; Kintl, A.; Mezera, J.; Hammerschmiedt, T.; Sobotková, J.; Brtnický, M.; Elbl, J. Using UAV to identify the optimal vegetation index for yield prediction of oil seed rape (*Brassica napus* L.) at the flowering stage. *Remote Sens.* **2022**, *14*, 4953. [CrossRef]
12. Zhang, T.; Vail, S.; Duddu, H.S.; Parkin, I.A.; Guo, X.; Johnson, E.N.; Shirtliffe, S.J. Phenotyping flowering in canola (*Brassica napus* L.) and estimating seed yield using an unmanned aerial vehicle-based imagery. *Front. Plant Sci.* **2021**, *12*, 686332. [CrossRef] [PubMed]
13. Zhang, Y.; Xia, C.; Zhang, X.; Cheng, X.; Feng, G.; Wang, Y.; Gao, Q. Estimating the maize biomass by crop height and narrowband vegetation indices derived from UAV-based hyperspectral images. *Ecol. Indic.* **2021**, *129*, 107985. [CrossRef]
14. Sapkota, S.; Paudyal, D.R. Growth monitoring and yield estimation of maize plant using unmanned aerial vehicle (UAV) in a hilly region. *Sensors* **2023**, *23*, 5432. [CrossRef] [PubMed]
15. Liu, Y.; Liu, S.; Li, J.; Guo, X.; Wang, S.; Lu, J. Estimating biomass of winter oilseed rape using vegetation indices and texture metrics derived from UAV multispectral images. *Comput. Electron. Agric.* **2019**, *166*, 105026. [CrossRef]
16. Fu, Z.; Jiang, J.; Gao, Y.; Krienke, B.; Wang, M.; Zhong, K.; Cao, Q.; Tian, Y.; Zhu, Y.; Cao, W.; et al. Wheat growth monitoring and yield estimation based on multi-rotor unmanned aerial vehicle. *Remote Sens.* **2020**, *12*, 508. [CrossRef]
17. Fu, H.; Wang, C.; Cui, G.; She, W.; Zhao, L. Ramie yield estimation based on UAV RGB images. *Sensors* **2021**, *21*, 669. [CrossRef] [PubMed]
18. Stroppiana, D.; Fava, F.; Boschetti, M.; Brivio, P.A. Estimation of nitrogen content in crops and pastures using hyperspectral vegetation indices. In *Hyperspectral Remote Sensing of Vegetation*; Thenkabail, P.S., Lyon, J.G., Huete, A., Eds.; CRC Press: Boca Raton, FL, USA, 2011; pp. 245–262.
19. Mutanga, O.; Skidmore, A.K. Narrow band vegetation indices overcome the saturation problem in biomass estimation. *Int. J. Remote Sens.* **2004**, *25*, 3999–4014. [CrossRef]
20. Gnyp, M.L.; Miao, Y.; Yuan, F.; Ustin, S.L.; Yu, K.; Yao, Y.; Huang, S.; Bareth, G. Hyperspectral canopy sensing of paddy rice aboveground biomass at different growth stages. *Field Crop. Res.* **2014**, *155*, 42–55. [CrossRef]
21. Fang, S.; Tang, W.; Peng, Y.; Gong, Y.; Dai, C.; Chai, R.; Liu, K. Remote estimation of vegetation fraction and flower fraction in oilseed rape with unmanned aerial vehicle data. *Remote Sens.* **2016**, *8*, 416. [CrossRef]
22. Li, L.; Tao, K.; Wang, S. Prediction models of winter oilseed rape yield based on hyperspeetral data at pod-filling stage. *Trans. Chin. Soc. Agric. Mach.* **2017**, *48*, 221–229.
23. Katsigiannis, P.; Misopolinos, L.; Liakopoulos, V.; Alexandridis, T.K.; Zalidis, G. An autonomous multi-sensor UAV system for reduced-input precision agriculture applications. In Proceedings of the 2016 24th Mediterranean Conference on Control and Automation (MED), Athens, Greece, 21–24 June 2016; pp. 60–64.
24. Barrile, V.; Simonetti, S.; Citroni, R.; Fotia, A.; Bilotta, G. Experimenting agriculture 4.0 with sensors: A data fusion approach between remote sensing, UAVs and self-driving tractors. *Sensors* **2022**, *22*, 7910. [CrossRef] [PubMed]
25. Wu, Q.; Zhang, Y.; Xie, M.; Zhao, Z.; Yang, L.; Liu, J.; Hou, D. Estimation of Fv/Fm in spring wheat using UAV-Based multispectral and RGB imagery with multiple machine learning methods. *Agronomy* **2023**, *13*, 1003. [CrossRef]
26. Wan, L.; Cen, H.; Zhu, J.; Zhang, J.; Zhu, Y.; Sun, D.; Du, X.; Zhai, L.; Weng, H.; Li, Y.; et al. Grain yield prediction of rice using multi-temporal UAV-based RGB and multispectral images and model transfer—A case study of small farmlands in the South of China. *Agric. For. Meteorol.* **2020**, *291*, 108096. [CrossRef]
27. Jełowicki, Ł.; Sosnowicz, K.; Ostrowski, W.; Osińska-Skotak, K.; Bakuła, K. Evaluation of rapeseed winter crop damage using UAV-based multispectral imagery. *Remote Sens.* **2020**, *12*, 2618. [CrossRef]
28. Motohka, T.; Nasahara, K.N.; Oguma, H.; Tsuchida, S. Applicability of green-red vegetation index for remote sensing of vegetation phenology. *Remote Sens.* **2010**, *2*, 2369–2387. [CrossRef]
29. Gitelson, A.A.; Viña, A.; Arkebauer, T.J.; Rundquist, D.C.; Keydan, G.; Leavitt, B. Remote estimation of leaf area index and green leaf biomass in maize canopies. *Geophys. Res. Lett.* **2003**, *30*. [CrossRef]
30. Hunt, E.R., Jr.; Doraiswamy, P.C.; McMurtrey, J.E.; Daughtry, C.S.; Perry, E.M.; Akhmedov, B. A visible band index for remote sensing leaf chlorophyll content at the canopy scale. *Int. J. Appl. Earth Obs. Geoinf.* **2013**, *21*, 103–112.29. [CrossRef]
31. Woebbecke, D.M.; Meyer, G.E.; Von Bargen, K.; Mortensen, D.A. Color indices for weed identification under various soil, residue, and lighting conditions. *Trans. ASAE* **1995**, *38*, 259–269. [CrossRef]
32. Hasan, U.; Sawut, M.; Chen, S. Estimating the leaf area index of winter wheat based on unmanned aerial vehicle RGB-image parameters. *Sustainability* **2019**, *11*, 6829. [CrossRef]
33. Cen, H.; Wan, L.; Zhu, J.; Li, Y.; Li, X.; Zhu, Y.; Weng, H.; Wu, W.; Yin, W.; Xu, C.; et al. Dynamic monitoring of biomass of rice under different nitrogen treatments using a lightweight UAV with dual image-frame snapshot cameras. *Plant Methods* **2019**, *15*, 32. [CrossRef]
34. Gitelson, A.A.; Kaufman, Y.J.; Stark, R.; Rundquist, D. Novel algorithms for remote estimation of vegetation fraction. *Remote Sens. Environ.* **2002**, *80*, 76–87. [CrossRef]
35. Du, M.; Noguchi, N. Monitoring of wheat growth status and mapping of wheat yield's within-field spatial variations using color images acquired from UAV-camera system. *Remote Sens.* **2017**, *9*, 289. [CrossRef]

36. Verrelst, J.; Schaepman, M.E.; Koetz, B.; Kneubühler, M. Angular sensitivity analysis of vegetation indices derived from CHRIS/PROBA data. *Remote Sens. Environ.* **2008**, *112*, 2341–2353. [CrossRef]
37. Bendig, J.; Yu, K.; Aasen, H.; Bolten, A.; Bennertz, S.; Broscheit, J.; Gnyp, M.L.; Bareth, G. Combining UAV-based plant height from crop surface models, visible, and near infrared vegetation indices for biomass monitoring in barley. *Int. J. Appl. Earth Obs. Geoinf.* **2015**, *39*, 79–87. [CrossRef]
38. Torres-Sánchez, J.; Peña, J.M.; de Castro, A.I.; López-Granados, F. Multi-temporal mapping of the vegetation fraction in early-season wheat fields using images from UAV. *Comput. Electron. Agric.* **2014**, *103*, 104–113. [CrossRef]
39. Hague, T.; Tillett, N.D.; Wheeler, H.J.P.A. Automated crop and weed monitoring in widely spaced cereals. *Precis. Agric.* **2006**, *7*, 21–32. [CrossRef]
40. Meyer, G.E.; Neto, J.C. Verification of color vegetation indices for automated crop imaging applications. *Comput. Electron. Agric.* **2008**, *63*, 282–293. [CrossRef]
41. Guijarro, M.; Pajares, G.; Riomoros, I.; Herrera, P.J.; Burgos-Artizzu, X.P.; Ribeiro, A. Automatic segmentation of relevant textures in agricultural images. *Comput. Electron. Agric.* **2011**, *75*, 75–83. [CrossRef]
42. Guerrero, J.M.; Pajares, G.; Montalvo, M.; Romeo, J.; Guijarro, M. Support vector machines for crop/weeds identification in maize fields. *Expert Syst. Appl.* **2012**, *39*, 11149–11155. [CrossRef]
43. Jordan, C.F. Derivation of leaf-area index from quality of light on the forest floor. *Ecology* **1969**, *50*, 663–666. [CrossRef]
44. Rouse, J.W.; Haas, R.H.; Schell, J.A.; Deering, D.W. Monitoring vegetation systems in the Great Plains with ERTS. *NASA Spec. Publ.* **1974**, *351*, 309.
45. Jiang, Z.; Huete, A.R.; Didan, K.; Miura, T. Development of a two-band enhanced vegetation index without a blue band. *Remote Sens. Environ.* **2008**, *112*, 3833–3845. [CrossRef]
46. Rondeaux, G.; Steven, M.; Baret, F. Optimization of soil-adjusted vegetation indices. *Remote Sens. Environ.* **1996**, *55*, 95–107. [CrossRef]
47. Huete, A.R. A soil-adjusted vegetation index (SAVI). *Remote Sens. Environ.* **1988**, *25*, 295–309. [CrossRef]
48. Roujean, J.L.; Breon, F.M. Estimating PAR absorbed by vegetation from bidirectional reflectance measurements. *Remote Sens. Environ.* **1995**, *51*, 375–384. [CrossRef]
49. Chen, J.M. Evaluation of vegetation indices and a modified simple ratio for boreal applications. *Can. J. Remote Sens.* **1996**, *22*, 229–242. [CrossRef]
50. Qi, J.; Chehbouni, A.; Huete, A.R.; Kerr, Y.H.; Sorooshian, S. A modified soil adjusted vegetation index. *Remote Sens. Environ.* **1994**, *48*, 119–126. [CrossRef]
51. Inoue, Y.; Sakaiya, E.; Zhu, Y.; Takahashi, W. Diagnostic mapping of canopy nitrogen content in rice based on hyperspectral measurements. *Remote Sens. Environ.* **2012**, *126*, 210–221. [CrossRef]
52. Zarco-Tejada, P.J.; Berni, J.A.; Suárez, L.; Sepulcre-Cantó, G.; Morales, F.; Miller, J.R. Imaging chlorophyll fluorescence with an airborne narrow-band multispectral camera for vegetation stress detection. *Remote Sens. Environ.* **2009**, *113*, 1262–1275. [CrossRef]
53. Zualkernan, I.; Abuhani, D.A.; Hussain, M.H.; Khan, J.; ElMohandes, M. Machine learning for precision agriculture using imagery from unmanned aerial vehicles (uavs): A survey. *Drones* **2023**, *7*, 382. [CrossRef]
54. Shahi, T.B.; Xu, C.Y.; Neupane, A.; Guo, W. Machine learning methods for precision agriculture with UAV imagery: A review. *Electron. Res. Arch.* **2022**, *30*, 4277–4317. [CrossRef]
55. Zhu, Y.; Liu, K.; Liu, L.; Myint, S.W.; Wang, S.; Liu, H.; He, Z. Exploring the potential of worldview-2 red-edge band-based vegetation indices for estimation of mangrove leaf area index with machine learning algorithms. *Remote Sens.* **2017**, *9*, 1060. [CrossRef]
56. Paleari, L.; Movedi, E.; Vesely, F.M.; Invernizzi, M.; Piva, D.; Zibordi, G.; Confalonieri, R. Estimating plant nitrogen content in tomato using a smartphone. *Field Crop. Res.* **2022**, *284*, 108564. [CrossRef]
57. Li, J.; Huang, W.; Zhao, C.; Zhang, B. A comparative study for the quantitative determination of soluble solids content, pH and firmness of pears by Vis/NIR spectroscopy. *J. Food Eng.* **2013**, *116*, 324–332. [CrossRef]
58. Zhu, H.; Chu, B.; Zhang, C.; Liu, F.; Jiang, L.; He, Y. Hyperspectral imaging for presymptomatic detection of tobacco disease with successive projections algorithm and machine-learning classifiers. *Sci. Rep.* **2017**, *7*, 4125. [CrossRef] [PubMed]
59. Zhu, H.; Chu, B.; Fan, Y.; Tao, X.; Yin, W.; He, Y. Hyperspectral imaging for predicting the internal quality of kiwifruits based on variable selection algorithms and chemometric models. *Sci. Rep.* **2017**, *7*, 7845. [CrossRef] [PubMed]
60. Gronowski, A.M.; Wong, E.C.; Wilhite, T.R.; Martin, D.L.; Smith, C.H.; Parvin, C.A.; Landt, M. Detection of glutamic acid decarboxylase autoantibodies with the varelisa ELISA. *Clin. Chem.* **1995**, *41*, 1532–1534. [CrossRef]
61. Mouazen, A.M.; Kuang, B.; De Baerdemaeker, J.; Ramon, H. Comparison among principal component, partial least squares and back propagation neural network analyses for accuracy of measurement of selected soil properties with visible and near infrared spectroscopy. *Geoderma* **2010**, *158*, 23–31. [CrossRef]
62. Wythoff, B.J. Backpropagation neural networks: A tutorial. *Chemom. Intell. Lab. Syst.* **1993**, *18*, 115–155. [CrossRef]
63. Mansoori, E.G.; Sara, M. Extreme ensemble of extreme learning machines. *Stat. Anal. Data Min. ASA Data Sci. J.* **2021**, *14*, 116–128. [CrossRef]
64. Han, H.G.; Ma, M.L.; Qiao, J.F. Accelerated gradient algorithm for RBF neural network. *Neurocomputing* **2021**, *441*, 237–247. [CrossRef]
65. Leardi, R. Application of genetic algorithm–PLS for feature selection in spectral data sets. *J. Chemom.* **2000**, *14*, 643–655. [CrossRef]

66. Gu, Q.; Sheng, L.; Zhang, T.; Lu, Y.; Zhang, Z.; Zheng, K.; Zhou, H. Early detection of tomato spotted wilt virus infection in tobacco using the hyperspectral imaging technique and machine learning algorithms. *Comput. Electron. Agric.* **2019**, *167*, 105066. [CrossRef]
67. Weber, V.S.; Araus, J.L.; Cairns, J.E.; Sanchez, C.; Melchinger, A.E.; Orsini, E. Prediction of grain yield using reflectance spectra of canopy and leaves in maize plants grown under different water regimes. *Field Crop. Res.* **2012**, *128*, 82–90. [CrossRef]
68. Xie, C.; Shao, Y.; Li, X.; He, Y. Detection of early blight and late blight diseases on tomato leaves using hyperspectral imaging. *Sci. Rep.* **2015**, *5*, 16564. [CrossRef]
69. Zhang, X.; Liu, F.; He, Y.; Gong, X. Detecting macronutrients content and distribution in oilseed rape leaves based on hyperspectral imaging. *Biosyst. Eng.* **2013**, *115*, 56–65. [CrossRef]
70. Hansen, P.M.; Schjoerring, J.K. Reflectance measurement of canopy biomass and nitrogen status in wheat crops using normalized difference vegetation indices and partial least squares regression. *Remote Sens. Environ.* **2003**, *86*, 542–553. [CrossRef]
71. Maimaitijiang, M.; Ghulam, A.; Sidike, P.; Hartling, S.; Maimaitiyiming, M.; Peterson, K.; Shavers, E.; Fishman, J.; Peterson, J.; Kadam, S.; et al. Unmanned Aerial System (UAS)-based phenotyping of soybean using multi-sensor data fusion and extreme learning machine. *ISPRS J. Photogramm. Remote Sens.* **2017**, *134*, 43–58. [CrossRef]
72. Gitelson, A.A.; Merzlyak, M.N. Remote sensing of chlorophyll concentration in higher plant leaves. *Adv. Space Res.* **1998**, *22*, 689–692. [CrossRef]
73. Zhang, L.; Niu, Y.; Zhang, H.; Han, W.; Li, G.; Tang, J.; Peng, X. Maize canopy temperature extracted from UAV thermal and RGB imagery and its application in water stress monitoring. *Front. Plant Sci.* **2019**, *10*, 1270. [CrossRef] [PubMed]
74. Haboudane, D.; Miller, J.R.; Tremblay, N.; Zarco-Tejada, P.J.; Dextraze, L. Integrated narrow-band vegetation indices for prediction of crop chlorophyll content for application to precision agriculture. *Remote Sens. Environ.* **2002**, *81*, 416–426. [CrossRef]
75. Ashapure, A.; Jung, J.; Chang, A.; Oh, S.; Maeda, M.; Landivar, J. A comparative study of RGB and multispectral sensor-based cotton canopy cover modelling using multi-temporal UAS data. *Remote Sens.* **2019**, *11*, 2757. [CrossRef]
76. Zheng, H.; Cheng, T.; Li, D.; Zhou, X.; Yao, X.; Tian, Y.; Cao, W.; Zhu, Y. Evaluation of RGB, color-infrared and multispectral images acquired from unmanned aerial systems for the estimation of nitrogen accumulation in rice. *Remote Sens.* **2018**, *10*, 824. [CrossRef]
77. Li, D.; Li, C.; Yao, Y.; Li, M.; Liu, L. Modern imaging techniques in plant nutrition analysis: A review. *Comput. Electron. Agric.* **2020**, *174*, 105459. [CrossRef]
78. Li, W.; Pan, K.; Liu, W.; Xiao, W.; Ni, S.; Shi, P.; Chen, X.; Li, T. Monitoring Maize Canopy Chlorophyll Content throughout the Growth Stages Based on UAV MS and RGB Feature Fusion. *Agriculture* **2024**, *14*, 1265. [CrossRef]
79. Chianucci, F.; Disperati, L.; Guzzi, D.; Bianchini, D.; Nardino, V.; Lastri, C.; Rindinella, A.; Corona, P. Estimation of canopy attributes in beech forests using true colour digital images from a small fixed-wing UAV. *Int. J. Appl. Earth Obs. Geoinf.* **2016**, *47*, 60–68. [CrossRef]
80. Zamani-Noor, N.; Feistkorn, D. Monitoring growth status of winter oilseed rape by NDVI and NDYI derived from UAV-based Red–Green–Blue imagery. *Agronomy* **2022**, *12*, 2212. [CrossRef]
81. Yang, Y.; Wei, X.; Wang, J.; Zhou, G.; Wang, J.; Jiang, Z.; Zhao, J.; Ren, Y. Prediction of Seedling Oilseed Rape Crop Phenotype by Drone-Derived Multimodal Data. *Remote Sens.* **2023**, *15*, 3951. [CrossRef]